Synthesis and catalytic performances of K-OMS-2, Fe/K-OMS-2 and Fe-K-OMS-2 in post plasma-catalysis for dilute TCE abatement

Sharmin Sultana a,∗, Zhiping Ye a,b, Savita K.P. Veerapandian a , Axel Löfberg b, Nathalie De Geyter a ,Rino Morent a , Jean-Marc Giraudon b,∗, Jean-François Lamonier b

a Ghent University, Faculty of Engineering, Department of Applied Physics, Research Unit Plasma Technology, Sint-Pietersnieuwstraat 41, 9000 Ghent, Belgium

b Univ. Lille, CNRS, Centrale Lille, ENSCL, Univ. Artois, UMR 8181 − UCCS − Unité de Catalyse et Chimie du Solide, F-59000 Lille, France

A B S T R A C T

Fe-doped manganese oxide octahedral molecular sieves (referred as OMS-2) of cryptomelane type structure were synthesized by co-precipitation and impregnation by refluxing at ambient pressure. The influence of Fe in the MnO 2 structure was assessed by several characterization techniques such as ICP-OES (inductively coupled plasma-optic emission spectroscopy), X-ray diffraction, Raman spectroscopy, N 2 adsorption analysis, H2 –TPR (hydrogen temperature programmed reduction), and TGA/DTA (Thermogravimetric analysis/Differential thermal analysis). The co-precipitated sample (Fe-K-OMS-2) shows better performances for TCE removal in moist air when used downstream from a NTP (non thermal plasma) generated in a DC multi-pin-to-plate corona/glow discharge in comparison to the iron free manganese oxide octahedral sieve (K-OMS-2). The enhanced performances towards TCE removal using Fe-K-OMS-2 downstream from the NTP are attributed to high surface oxygen mobility and to an increase of structural defects resulting from improved textural properties. These characteristics allow promoting O3 decomposition and TCE catalytic total oxidation (CTO) efficiencies.

1. Introduction

A large and important group of air pollutants consists of Volatile Organic Compounds (VOCs) which particularly harm human health and our environment. Along with carcinogenic and mutagenic effects on human health [1], VOCs are also precursors to ground level ozone which is principally responsible for photochemical smog. The research of innovative technologies for VOC abatement is stimulated to accommodate the new stringent standards in terms of VOC emission. One emerging strategy is the coupling of 2 existing complementary technologies, namely here Non Thermal Plasma (NTP) and Catalytic Total Oxidation (CTO), to get a more efficient process for VOC removal in air. Indeed although NTP displays a high reactivity in air towards VOC removal at atmospheric pressure and ambient temperature, it has however a low CO2 selectivity currently producing other VOC by-products, CO, and hazardous ozone. This lack of CO2 selectivity can be overcome by the addition of a O 3 decomposition/VOC total oxidation catalyst downstream of the plasma discharge to form a post plasma-catalysis (PPC) system [2–4]. Here the catalyst takes advantage of its high efficiency towards the destruction of ozone to give active species able to oxidize the plasma processed hazardous by-products and the possibly remaining VOC into CO2.

The performances of NTP in PPC have already been investigated in particular for trichloroethylene (TCE) removal which is a very reactive molecule towards cold plasma in dry/wet air [5–7]. Indeed TCE is recognized as a highly toxic chlorinated VOC widely used in industry as metal degreasing agent. The design of the catalyst has to be performed taking into account some basic requirements such as ozone

decomposition ability, VOC total oxidation capacity, as well as hydrothermal stability and resistance to chlorine. Among the different catalysts already investigated MnO 2 appears to be very interesting, especially, due to its very high activity towards O3 degradation [8]. However MnO2 shows various crystallographic phases. Cryptomelane, an octahedral molecular sieve (OMS) is one allotropic form of MnO 2 having a (2 × 2) tunnel structure (OMS-2). The structure is made of the superposition of 4 units of 2 edged MnO 6 octahedra building blocks connected by corners along the c axis forming 1D microporous square tunnel of 0.46 nm in size. K + cations which are located inside the (2 × 2) tunnels provide charge balance and stabilize the structure (K-OMS-2; general formula K x Mn8 O 16 with an average manganese oxidation of about 3.8). The open structure of the channels, the easy cycling of Mn4+ /Mn 3+ and the high mobility of lattice oxygen as well as more recently the morphology of the particles have been put forward as important characteristics to take into account for their activity in CTO of VOCs [9–18]. On purpose MnO2 oxides have been already shown interesting TCE abatement properties in PPC [6,7,19,20]. The TCE total oxidation performed in moist air in the presence of CO 2 was previously investigated as a function of energy density using an atmospheric pressure negative DC luminescent glow discharge combined with a cryptomelane catalyst positioned downstream from the plasma reactor [19,20]. The ability of the catalyst to decompose plasma generated ozone allows getting active oxygen species enabling the destruction of plasma generated polychlorinated hazards and the enhancement of TCE abatement. The main limitation is the side formation of some C1 chlorinated compounds believed to be in line with a partial chlorination of the catalyst when the temperature of the catalyst is to low [19,20]. In order to promote the efficiency of the PPC process towards VOC abatement a possible strategy is to improve the physical and catalytic properties of K-OMS-2 material by doping. Indeed doping of single–type, low or high-valent metal transition cations, has been previously showed to produce cryptomelane with novel morphologies [21] and improved catalytic properties [22]. Doping cryptomelane with various cations of different types can improve the textural properties [23,24], modify Mn average oxidation state (AOS) [9,25,26] and thermal stability [9,23,26,27], increase structural defects, e.g., vacancies [23,27], and also enhance the reactivity of cryptomelane towards the catalytic oxidation of various organic pollutants [24,28–30]. It follows from these considerations that the physico-chemical properties of the metal doped K-OMS-2 depend on the nature of the doping metal and of the synthesis conditions, such as among others, through the mode of incorporation and temperature of calcination of the oxide precursor material. As a result the doping cation can be incorporated into the channels, partially replacing K+ ions and/or substitute M 3+ or Mn 4+ cations in MnO 6 octahedra and/or be present as dispersed transition metal oxides supported on the cryptomelane phase [23]. Among the possible transition metal dopants Fe has been chosen as it has been previously reported that Mn-Fe oxides may be promising catalysts for ozone decomposition [31]. Taking advantage of this property, Mn-Fe oxides dispersed on cordierite have been recently used successfully in a PPC process for the decomposition of diethylether [32]. Additionally Fe doped cryptomelane catalysts have been reported to enhance VOC total oxidation [33]. Reported Fe-doped cryptomelane synthesis methods include hydrothermal treatment of Fe-doped layered birnessite [9], redox precipitation under reflux [34], sol–gel assisted combustion methods [26], addition of iron precursor to cryptomelane and heating [33].This present study focuses on the preparation, characterization and evaluation in TCE oxidation (in presence of moist air) of Fe-doped K-OMS-2 oxides placed downstream from a NTP reactor prepared by introduction of Fe either by co-precipitation [34] or by deposition of Fe(OH) x (x = 2-3) over the K-OMS-2 solid [35] prepared by the reflux method in order to modify the chemical/physical properties of the catalysts.

2. Materials and methods

2.1. Catalyst preparation

The introduction of iron to cryptomelane was performed by 2 different ways inspired by literature: (i) by co-precipitation followed by calcination at 450 °C (Fe-K-OMS-2) [34]; (ii) by deposition of Fe(OH) x(x = 2; 3) over K-OMS-2 followed by calcination at 450 °C (Fe/K-OMS-2) [35]. A reference cryptomelane (K-OMS-2) was also synthesized.

2.1.1. Synthesis of K-OMS-2

A KMnO 4 (Fluka, 99%; 6.385 g in 150 mL; n Mn(II) ≈ 1.5 n Mn(VII)) solution was added dropwise to manganese (II) acetate (Mn(CH 3CO 2) 2 · 4H 2O; Prolabo, 99%; 14.854 g in 50 mL) dissolved in a CH 3COOH/CH3COOK buffer solution of pH 4.5 while stirring. A black brown precipitate was rapidly formed and the mixture was stirred 24 h at reflux. The precipitate was then washed thoroughly with distilled water and dried overnight at 100 °C. The resulting powder was calcinated at 450 °C for 4 h (1 °C/min) in air (0.3 L/min).

2.1.2. Synthesis of Fe-K-OMS-2

A KMnO 4 (Fluka, 99%; 6.98 g ≈ 0.044 mol in 80 mL) heated at 60 °C was added to an aqueous acidified solution (CH 3COOH; Alfa Aesar, 99%; 12 mL of a 2 mol/L solution into 90 mL of water) of Mn and Fe nitrate precursors ((Mn(NO 3) 2·4H 2O; Sigma-Aldrich, 97%; 11.76 g ≈ 0.045 mol) and Fe(Fe(NO 3)3 ·9H 2O; Fisher Scientific, 98%; 1.9 g ≈ 0.00461 mol)) to get a precipitate. The suspension was stirred vigorously at reflux for 20 min. An additional amount (≈8 mL) of 2 mol/L acetic acid was added to retrieve the volatilized acetic acid during reaction. The precipitate was separated through centrifugation and washed with deionized water several times until neutral pH, followed by drying at 100 °C for 12 h. The resulting solid was calcined in air (0.3 L/min) at 450 °C for 4 h (1 °C/min).

2.1.3. Synthesis of Fe/K-OMS-2

0.41 g of Fe(NO 3) 3·9H 2O (Fisher Scientific, 98%; ≈0.001 mol) and 0.40 g of (NH 4) 2Fe(SO 4) 2 ·6H 2O (Sigma-Aldrich, 98%; ≈0.001 mol) (n Fe(II) = n Fe(III)) were dissolved in 50 mL of water (pH = 2.6). A KOH (Sigma-Aldrich-85%) solution of 1 mol/L was added dropwise to the initial solution, under constant stirring, to a final pH of 9.6 allowing the successive precipitation of Fe(OH)x (x = 2,3). At that stage K-OMS-2 (n Fe/n Mn = 0.10) was introduced above this pH as powder to the aqueous suspension and KOH was again added dropwise until a pH of 12. The resulting solid was intensively washed with distilled water and dried before to be calcined at 450 °C for 2 h.

2.2. Catalyst characterization

K, Mn and Fe elemental analyses were performed by inductively coupled plasma-optic emission spectroscopy (ICP-OES) at the REALCAT platform (Lille University). The sample preparation was made by dissolving 10 mg of dried and ground solid in 1.5 mL of concentrated aqua regia solution. Solutions were heat at 50 °C and stirred during 12 h. All sample solutions were stirred and the volume was adjusted up to 50 mL with ultrapure water before being analyzed by ICP-OES.

X-ray diffractograms were recorded using a Bruker AXS D8 Advance diffractometer. Data were collected using the Cu Kα line in the 10–70° 2-theta range with a 0.02° 2 θ step and a counting time of 3 s per step. Crystallite size was estimated from the FWHM of the peak located at 2 θ= 28.9° using the Scherrer equation, after correction of the FWHM to account for the instrumental broadening using the Diffrac. EVA-crystallite size determination.

The Raman spectra of the samples were recorded at room temperature using a Raman microprobe (Labram HR) equipped with a Peltier-cooled detector. The exciting light source was the 488 nm line ofan Ar^{+}-ion laser and the spectral resolution was ± 1.5 cm−1.

The morphology of the materials was observed using Scanning Electron Microscopy images recorded on a Hitachi S-4700 apparatus.

The specific surface areas were determined using a conventional multipoints BET nitrogen adsorption method with a MicromeriticsTristar II apparatus. Prior to nitrogen adsorption, the samples were outgassed for 4 h at 150 °C under vacuum.

TGA analyses were performed on sample size of about 10 mg in air flow (50 mL/min) with a heating rate of 10 °C/min up to 800 °C using a TA Instruments TGA-SDT 2960.

Temperature programmed reduction (TPR) were carried out using a Micromeritics 2920 Autochem II Chemisorption Analyzer. 50 mg sample was put into a quartz U-shaped tubular quartz reactor. The samples were pre-treated in flowing Ar at 150 °C for 60 min followed by cooling down to room temperature. The reducing gas was a mixture of 5 vol.% H2 /Ar at a total flow rate of 50 mL/min. The temperature was allowed to increase from 25 °C to 800 °C with a heating rate of 10 °C/min.

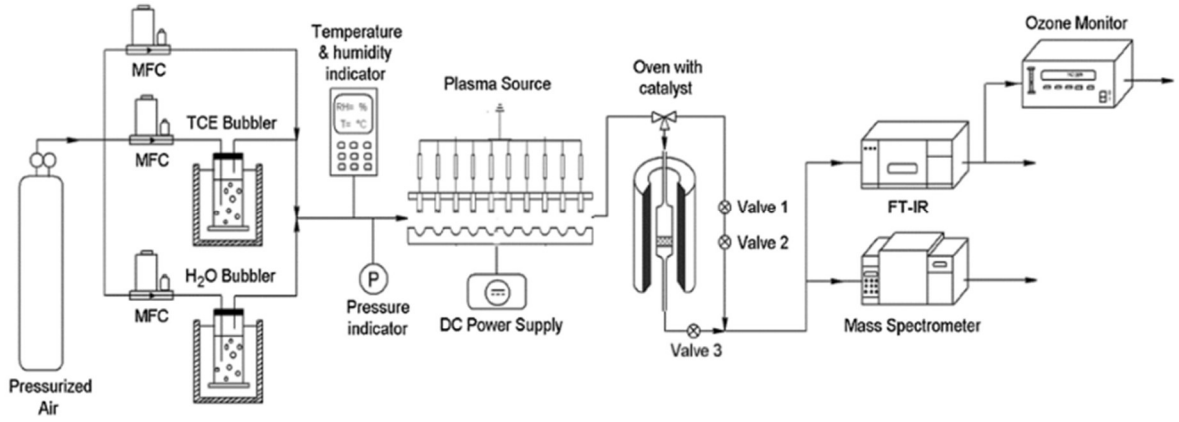

Fig. 1. Schematic diagram of the PPC experimental set-up.

2.3. Experimental set-up and experimental procedure

Fig. 1 shows the schematic diagram of the experimental set-up including a trichloroethylene generator, a plasma-catalysis reactor and an exhaust gas analysis section. Trichloroethylene (99.99% purity, A-CROS) was evaporated by bubbling with moist air (RH = 15%) and diluted with air before to be introduced into the plasma reactor. The flow rate and TCE concentration were adjusted by mass flow controllers (MFC) and fixed at 30 L/h and 300–350 ppmv, respectively. The 10-pin-to plate plasma reactor was similar to the one used before [36] except that the pin to plate modules were herein doubled. A negative DC corona/glow was used as discharge. A quartz tube filled with 0.5 g of catalyst diluted in 3 g of SiC (EMB 45053-Prolabo; 0.105 mm) pretreated with dry air at 350 °C for 4 h (12 L/h) was located downstream from the plasma reactor. The performances of the hybrid process toward TCE removal was assessed regarding the following sequence: the catalyst was first exposed to the reactive gas flow at 50 °C for 10 min. Then the plasma was turned on and after plasma stabilization of 5 min the energy density was allowed to increase by step of 30 J/L of 5 min duration from 30 J/L to 120 J/L. This sequence was repeated for catalyst temperatures of 100 and 150 °C (3 °C/min). The TCE abatement efficiency, COx and CO2 yields as well as the identification of by-products were determined using a FT-IR spectrometer (Bruker, Vertex 70) [37]. Ozone formation was analyzed by an UV ozone monitor (Envitec, model 450). To evaluate the efficiency of the process the following parameters were estimated:

The TCE abatement was calculated from :

$$TCE\ \text{Abatement}(\%) = \frac{[TCE]_{in} - [TCE]_{out}}{[TCE]_{in}} \times 100$$

where [TCE] in and [TCE] out were the concentration introduced in the reactor and that measured at the exit of the catalytic reactor, respectively. The CO yield, Y CO, and the CO2 yields, Y CO2, were calculated as follows:

$$Y_{CO}(\%) = \frac{[CO]_{out}}{2 \times [TCE]_{in}} \times 100 \quad (2)$$

$$Y_{CO_2}(\%) = \frac{[CO_2]_{out}}{2 \times [TCE]_{in}} \times 100 \quad (3)$$

3. Results and discussion

3.1. Main characteristics of the materials

3.1.1. Chemical analysis

The physico-chemical characterizations of the fresh materials are given in Table 1. A formula of K0.12 MnO2 was obtained for K-OMS-2sample based on the ICP-OES analysis. Charge balance calculation gives a Mn AOS of 3.88 which agrees with those of 3.87 [25] and of 3.89 [38,39] reported elsewhere for cryptomelane synthesized hydrothermally [25] or by reflux method [38,39], respectively. It is worth mentioning that in cryptomelane-type solid, Mn AOS usually varies between 3.6 and 3.8 in line with the mixed-valence Mn(IV) and Mn(III) structure [40]. Based on elemental analysis, the Fe/K-OMS-2 and Fe-K-OMS-2 samples exhibit Fe/Mn atomic ratios of 0.10 and 0.077, respectively, in perfect agreement with that present in the reaction mixture of 0.10 for the impregnated sample but at a slightly higher value for the co-impregnated sample (Fe/Mn ratio of 0.52 in solution). As expected Fe/K-OMS-2 oxide displays a comparable K/Mn ratio than that of K-OMS-2 in agreement with dispersion of iron based oxides over K-OMS-2 acting as the support. Conversely the K/Mn ratio of 0.027 is far less than that expected and shows that the mode of introduction of the dopant plays a key role in the nature of the final oxide.

3.1.2. Structural properties

The X-Ray diffraction patterns of K-OMS-2 and Fe/K-OMS-2 catalysts (Fig. 2) showed peaks which can be indexed to the tetragonal K-OMS-2 phase (JCPDS: 44-0141) (space group (I 4/m) with unit cellparameters a = b = 9.81 Å and c = 2.85 Å [41]. Furthermore the mean crystallite size keeps rather constant, of about 14–15 nm (Table 2), for both solids. Additional peaks located at 36.1° and 63.0°can be attributed to Fe-Mn spinels such as Fe (Fe 1.08Mn 0.92)O 4 (JCPDS 01-077-9278) or/and FeMn 2O 4 (JCPDS 04-006-9026), rather than maghemite (γ-Fe 2O 3) phase (JCPDS 13-0458), dispersed on cryptome-lane without discarding the possibility of segregated amorphous or/and low content Fe and/or Mn (hydroxy)oxide phases. Otherwise the XRD pattern of Fe-K-OMS-2 shows very broad envelopes of overlapping peaks of low intensity whose positions match those of K-OMS-2 to be

Table 1

Chemical composition of the fresh catalysts.

Catalysts	Mn	Fe	K	K/Mn	Fe/Mn	K/(Mn + Fe)
K-OMS-2	59.76	–	5.03	0.12	–	0.12
Fe/K-OMS-2	59.50	6.10	5.88	0.14	0.10	0.13
Fe-K-OMS-2	58.69	4.53	1.11	0.027	0.077	0.025

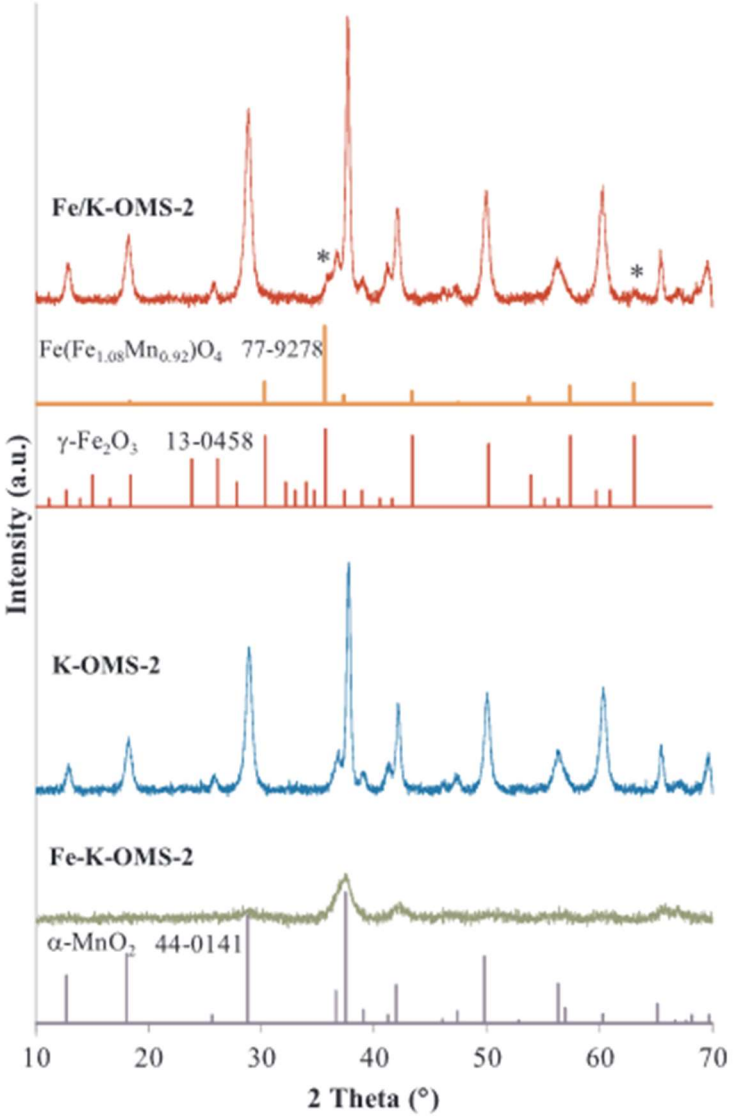

Fig. 2. XRD patterns of the synthesized materials.

consistent with the presence of a very disordered cryptomelane phase. The lattice vibrational behavior of both the undoped and Fe based K-OMS-2 materials was studied by Raman spectroscopy in order toprobe the effect of iron addition on the spectral features of the K-OMS-2 material (Fe/K-OMS-2), to validate the postulated formation of cryptomelane and check for the presence of segregated crystalline and/or amorphous metal oxides. OMS-2 type materials crystallize into a body centered tetragonal structure with a space group I4/m. Group theory predicts 15 Raman-active modes 6A g + 6B g + 3E g [42]. The Raman spectrum of K-OMS-2 displayed in Fig. 3 reveals only 9 characteristic peaks at 185, 280, 330, 386, 470, 512, 575, 630, and 745 cm−1 for the regular K-OMS-2 in good agreement with the data reported by Gao et al.[42]. The 2 most intense peaks at 574 and 634 cm−1 which have

been previously associated to Mn-O vibrations along and orthogonal to the direction of the MnO6 octahedral double chains (A g modes), respectively have been previously recognized to be the diagnostic of a well-developed tetragonal structure with 2 × 2 tunnels [42]. The Raman spectrum of Fe/K-OMS-2 shows these 2 characteristic lines but much enlarged than those of the K-OMS-2 oxide. Conversely the Raman contributions in the 200–400 cm−1 spectral region have almost disappeared and an apparent additional line is now observed at 556 cm−1 which can be due to the presence of segregated phases or/and different local environment of manganese.

3.1.3. Textural properties

The textural properties are significantly improved when adding Fe. In particular the BET specific surface increased 4 times and the pore volume 2 times for Fe-K-OMS-2 in comparison with K-OMS-2 (Table 2). The representative SEM image of K-OMS-2 solid which is similar to that of Fe/K-OMS-2 solids is displayed in Fig. 4a. The needle-like morphology is clearly observed (average length: 1 µm). Conversely the SEM image of the Fe-K-OMS-2 solid exhibits particles of pseudo-spherical morphology (average size: 300 nm) as shown in Fig. 4b. It turns out in that case that the elongation growth of the particles is partially inhibited. This observation may suggest some Fe incorporation into the Mn framework of cryptomelane as previously reported in the literature [34]. However the assignment of the exact position of Fe in the structure is a difficult task. Complementary experiments have to be implemented to assess the effect of the Fe addition on the location of Fe in the structure through isomorphic substitution of Mn^{n+} in the octahedral sites of Mn^{n+} or partial replacement of K+ into the tunnels of the structure.

3.1.4. Temperature programmed reduction (H 2-TPR)

Fig. 5 shows the TPR profiles of the materials. It is worthy to mention that the H2 consumption profile of K-OMS-2 shows a global envelope rather similar to those reported by T. Chen et al. and W. Y. Hernándeza et al. [43,44]. Four peaks at 300, 338, 356 and 374 °C can be seen. The lowest temperature reduction process has been previously attributed to the consumption of structural oxygen close to the surface leading to oxygen vacancies [44]. The three other ones are in line with a consecutive reduction scheme involving the successive steps:

MnO 2 − > Mn 2O 3 − > Mn3 O 4 − > MnO [45].

The peaks observed at 289, 325, 334, 338, and 365 °C in the Fe/K-OMS-2 solid were shifted to lower temperature in comparison to the K-OMS-2 oxide. The TPR profile appears more complex due to the additional reducibility of the Fe-Mn spinel dispersed on K-OMS-2, among others. By opposition the Fe-K-OMS-2 solid shows 3 contributions at 210, 277, and 301 °C in the low temperature range which are well separated from the peak at higher temperature (407 °C). It is worth mentioning that the temperature of the onset of reduction decreases as follow: K-OMS–2 > Fe/K-OMS–2 > Fe-K-OMS-2. The improved oxygen lability observed for Fe-K-OMS-2 may be related to many defects such as oxygen vacancies which would promote the degradation of the VOC and reaction intermediates. Table 2 lists the H 2 consumption of the different catalysts in the reduction process. The H2 consumptions of K-OMS-2, Fe/K-OMS-2 and Fe-KOMS2 are 9.90, 9.29, and 8.75 mmol/g, respectively. Based on the H2 consumption and the corresponding Mn content given in Table 1, the Mn AOS for K-OMS-2 by assuming MnO as final product [45] is calculated to be 3.82 in good agreement with the value of 3.88 obtained by ICP-OES. The Mn AOS of Fe/K-OMS-2 and Fe-KOMS2 are calculated to be 3.68 and 3.61, respectively, by assuming all iron in the

Table 2

Textural, structural and reducibility properties of the fresh catalysts

Catalysts	Textural properties			Redox properties		Thermal behavior		
	S_{BET} (m^2/g)	V_p[a] (cm^3/g)	dc[b] (nm)	H_2 (mmol/g)	Mn AOS	25–250 °C (%)	250–780 °C (%)	25–750 °C (%)
K-OMS-2	46	0.25	14.0	9.90	3.82	1.1	3.6	4.7
Fe/K-OMS-2	73	0.44	15.4	9.29	3.71	1.5	2.4	3.9
Fe-K-OMS-2	199	0.44	–	8.75	3.64	5.7	5.7	11.4

[a] Pore volume.
[b] Mean crystallite size.

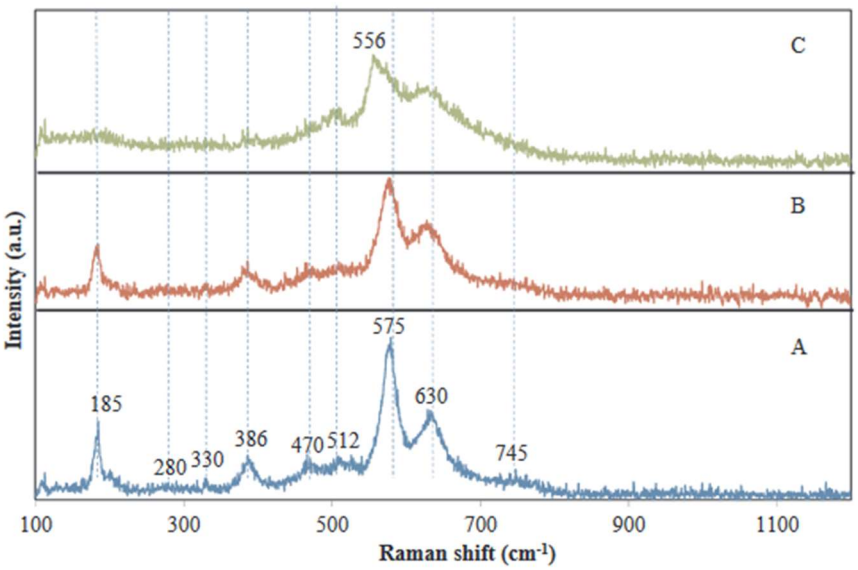

Fig. 3. Raman spectra of the synthesized materials (A: K-OMS-2; B: Fe/K-OMS-2; C: Fe- K-OMS-2).

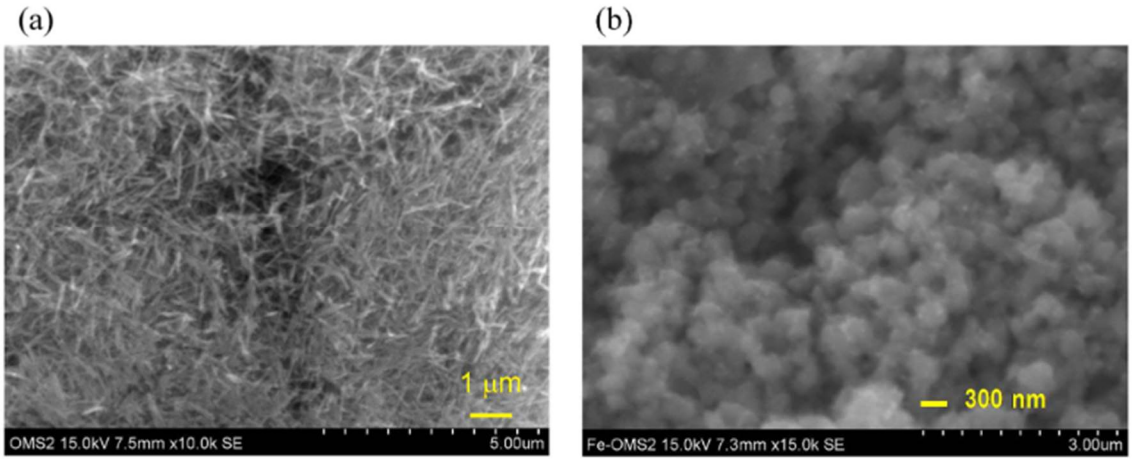

Fig. 4. Representative SEM images from (a) K-OMS-2 and (b) Fe-K-OMS-2 solid.

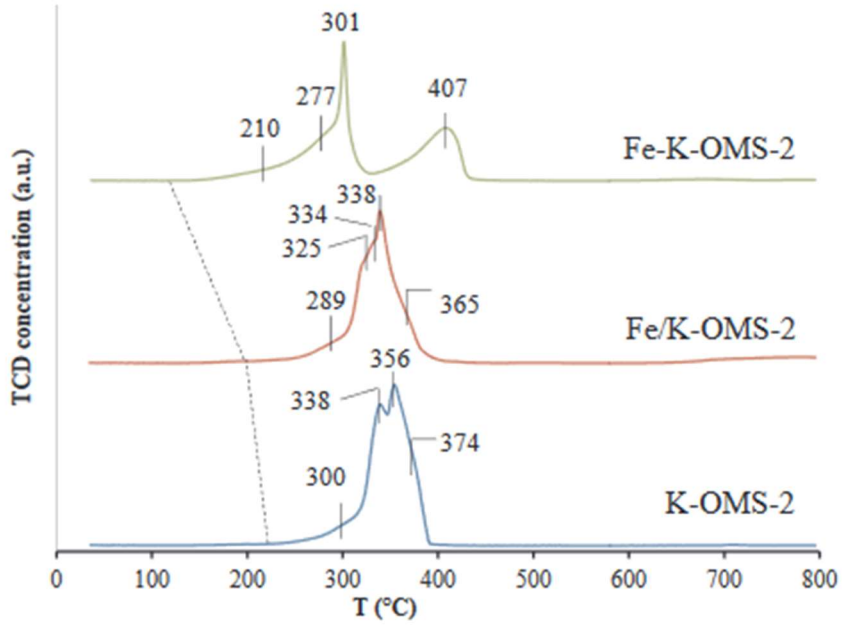

Fig. 5. H_2-TPR profiles for the synthesized materials.

samples to be Fe 3+ and by assuming Fe 3O 4 as the end product of reduction. As a result the Mn AOS decreases with the introduction of Fe. When considering Fe/K-OMS-2 the Mn AOS decrease is mostly due to the reduction of segregated Fe-Mn spinel species in accordance with XRD results. In a similar way segregated amorphous or well dispersed related Fe-Mn may also contribute to the Mn AOS decrease for Fe-K-OMS-2 sample.

3.1.5. Thermal stability

Thermal gravimetric analysis (TGA) and differential thermal analysis (DTA) profiles for the different solids performed in dry air are displayed in Fig. 6a-b and relevant results are in Table 2. The differential thermogravimetric (DTG) curves of K-OMS-2 and Fe/K-OMS-2 samples have similar behavior showing three separate steps in the temperature range of 25 °C– 800 °C. The two first steps at temperature up to 200 °C correspond to the elimination of physisorbed and chemisorbed water in different environments [46]. When the temperature exceeds 200 °C, the weight loss slows down until the temperature of about 500 °C. With the temperature increase up to 780 °C, the third weight loss which increases to 3.6 and 2.4% for K-OMS-2 and Fe/K-OMS-2, respectively, have been ascribed to the desorption of water inside the (2 × 2) channels as well as the departure of some structural oxygen close to the surface inducing oxygen vacancies without destroying the materials [47]. The removal of these species agree with the observance of an endothermic peak located at 642 and 673 °C for the free and iron containing oxide, respectively. In comparison with the two previous solids the DTA trace of Fe-KOMS-2 shows two weight loss steps in the range 25–200 °C and 400–550 °C to stabilize beyond 550 °C. As previously observed the first weight loss corresponds to the removal of water while the second weight loss is related to the crystallization of the solid consistently with DTA behavior.

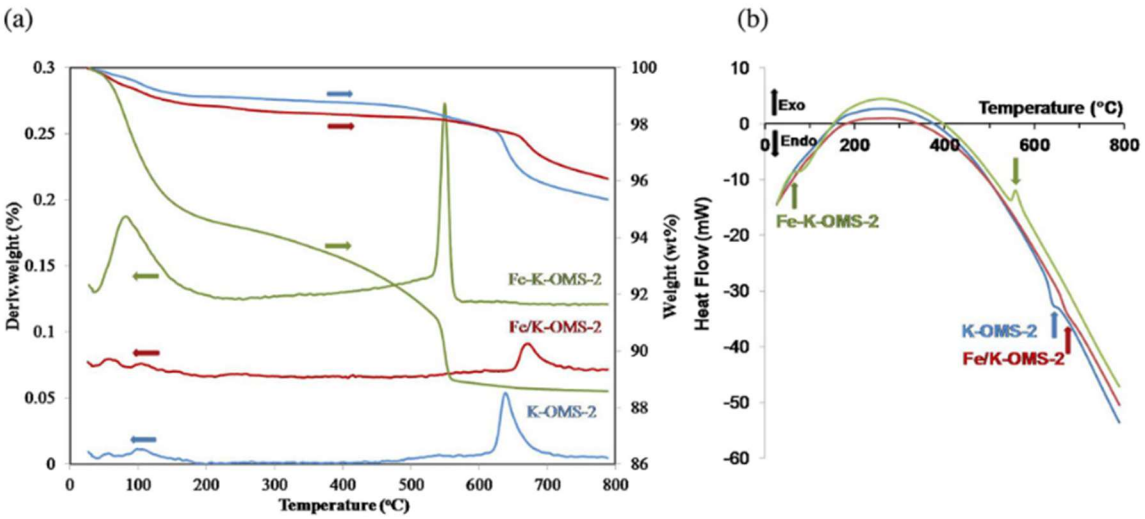

Fig. 6. (a) TGA/DTG and (b) DTA profiles as a function of temperature over the synthesized materials

4. Plasma-catalysis

4.1. Plasma alone

The performance of the NTP alone toward TCE abatement has been investigated as a function of energy density which is defined as the energy given by the plasma to 1 L of gaseous gas. The TCE conversion increases with ED due to the formation of more energetic electrons as shown in Fig. 7. The production of plasma generated ozone increases linearly with time to reach 150 ppmv at 120 J/L. The COx yield is low, about 15% (not shown), demonstrating the poor mineralization of TCE into CO 2. This is in line with the formation of polychlorinated by-products such as phosgene (PG), di-chloroacetylchloride (DCAC) and trichloroacetaldehyde (TCAD) identified from FT-IR spectra as previously reported [37].

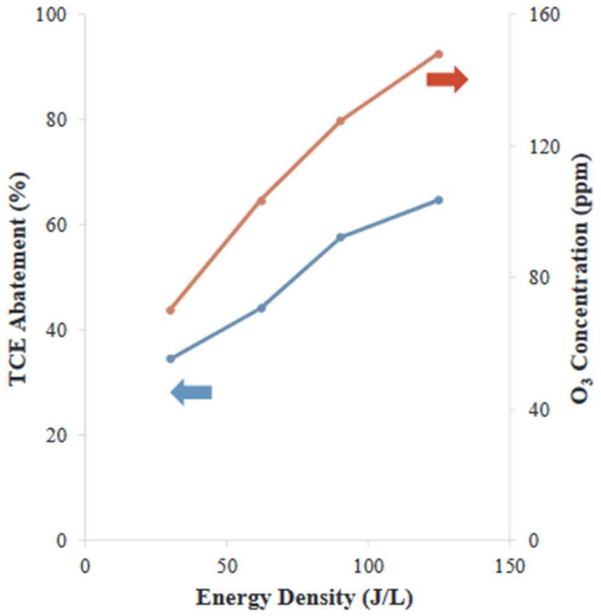

Fig. 7. TCE conversion and O3 production as a function of temperature with NTP alone.

4.2. Post plasma-catalysis

Figs. 8 and 9show the evolution of TCE abatement and CO 2 yield as a function of energy density (ED) for the 3 catalysts working in post-plasma configuration compared to those of NTP alone. First of all with plasma turn off, at a catalyst temperature (Tc) of 50 °C, it is observed 62% TCE abatement over Fe-K-OMS-2 oxide in comparison with the 2 other catalysts for which the TCE abatement is close to zero. This is explained by the high surface area of the catalyst enabling to retain a high amount of TCE in agreement with a CO2 yield close to zero. When the surface of the catalyst would be saturated with the VOC a decrease in TCE conversion would be expected to occur. With plasma turn on, the TCE conversion was less than that of NTP at ED of 30 J/L suggesting that the downstream catalyst was working in unsteady-state conditions. At higher ED the TCE conversion profiles as a function of ED over K-OMS-2 and Fe-K-OMS-2 catalysts behave similarly with that of NTP.This clearly indicates that only NTP is responsible for TCE degradation. Although the TCE conversion is much higher than that of NTP for PPC-Fe/K-OMS-2 process no CO2 yield improvement was observed in a comparison with the two other PPC configurations. However, whatever the catalyst under concern, the CO 2 yield values at 120 J/L of about 20% (Fig. 9) are higher than the C 2 yield value for NTP of about 4.6%. When the temperature of the catalyst is allowed to increase to 100 °C the physical TCE adsorption over the catalysts can now be neglected. With plasma turn off, it was noticed a CO 2 yield of 52% at 38% TCE conversion for PPC-Fe-K-OMS-2 configuration. The TCE conversion was observed to continuously increase with ED up to 88% at ED of 120 J/L while the CO2 yield globally decreases to reach an ending value of 43%. Conversely both TCE conversion and CO 2 yields increase with energy density when taking into account the two other configurations. Additionally, it is worthy to mention that CO is the main gaseous by-product of the reaction. In terms of increasing CO 2 and CO x (x = 1–2) yields the hybrid processes can be ranked as follow (Tc: 100 °C; ED: 120 J/L): PPC-K-OMS-2 (33; 52) < PPC-Fe/K-OMS-2 (40; 58) < PPC-Fe-K-OMS-2 (44; 60). When the temperature of the catalyst is allowed to vary to 150 °C it is found once more an increase of TCE conversion and CO2 yield as a function of ED in PPC-K-OMS-2 and PPC-Fe/K-OMS-2 configurations. However, the beneficial effect of temperature on TCE conversion when rising the temperature from 100 °C to 150 °C is not so clear as it is only observed for

ED less and higher than 60 J/L for PPC-K-OMS-2 and PPC-Fe/K-OMS-2 processes, respectively. These results can be consistent with changes in the physical/chemical properties of the catalysts. Future work involving the study of catalyst stability in PPC configuration is necessary to establish such catalyst evolution. By opposition it is observed, at a catalyst temperature of 150 °C, a significant improvement in TCE abatement performances (TCE abatement: 78%; CO2 yield: 52%) over Fe-K-OMS-2 catalyst due to an efficient thermal activation. With plasma turn on, it is found that both TCE conversion and CO2 yield globally increase as a function of ED showing in that way the beneficial assistance of NTP. As a result, 63% of CO2 yield can be achieved for a TCE conversion close to 100%.

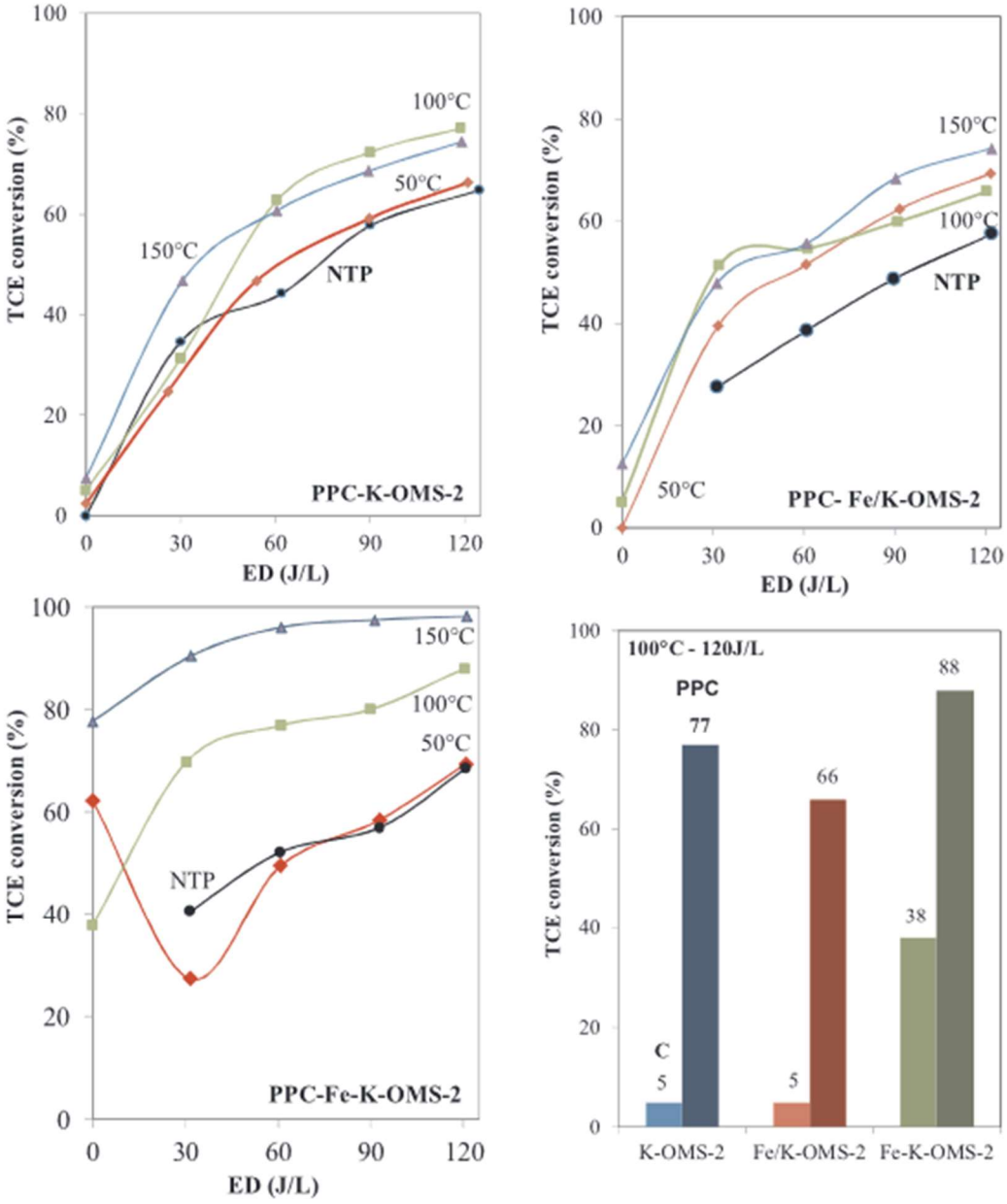

Fig. 8. TCE conversion in PPC experiments as a function of ED and catalyst temperature.

The efficiency of the PPC process towards TCE total oxidation in a comparison with that of NTP was assessed when looking at the FT-IR spectra of both the inlet and outlet stream recorded between 700 and 1100 cm−1 and 1720–1880 cm−1, respectively, (Fig. 10a-b) at Tc of 150 °C for an energy density of

90 J/L. With plasma turn on, the TCE decomposition is revealed by the decrease in intensity of the C-H out of plane deformation band of TCE at 945 cm−1 (Fig. 10a) while ozone production from dioxygen is detected in the outlet stream by bands at 1014–1046 cm−1 [48,49]. In the 1720–1880 cm−1 FT-IR window the characteristic bands at 1790 and 1820 cm−1 can be ascribed to the presence of dichloroacetylchloride (DCAC), that at 1830 cm−1 to phosgene (PG) and that at 1780 cm−1 to trichloroacetaldehyde (TCAD) (Fig. 10b) The detection and possible reaction schemes of formation of such intermediate oxidation products have already been observed and discussed elsewhere [36,37]. In PPC configuration the intensity of the band of TCE at 945 cm−1 decreases once more to almost disappears in the case of PPC-Fe-K-OMS-2. Whatever the PPC configuration, the bands relative to O 3 and polychlorinated compounds disappear while analysis of the different FT-IR spectra shows the emergence of new bands located at 795 and 774 cm−1 characteristic of the C-Cl bond vibration relative to CCl 4 and HCCl3, respectively [36]. HCCl3 and CCl4 formations can be explained by the reaction of CHCl 2 and CCl 3 radicals resulting from the easy cleavage of the carbon–carbon bond of DCAC and TCAD with adsorbed Cl. However, the intensity of these characteristic bands is minimized in PPC-Fe-K-OMS-2 configuration showing in that way the importance of the nature of the catalyst. These above observations attest of the beneficial role of ozone to give active oxygen species over the catalyst surface enabling the production of active species prone to oxidize the plasma processed gaseous polychlorinated by-products as well as the remaining TCE owing to the formal equations:

$$Cl_2CO + (5/3)O_3 \rightarrow CO_2 + Cl_2 + 2O_2$$

$$C_2Cl_3OH + (10/3)O_3 \rightarrow 2CO_2 + Cl_2 + HCl + 3.5O_23{\cdot}5O_2$$

$$C_2Cl_3H + 4O_3 \rightarrow 2CO_2 + Cl_2 + HCl + 4O_2$$

To sum-up, the introduction of iron by co-precipitation has a significant beneficial impact on the properties of the catalyst: K-OMS-2 like structure with many defects, particles of pseudo-spherical morphology, high specific surface area and an increase of the reducibility of surface Mn^{4+}. A possible interaction between Mn and Fe in the Fe-K-OMS-2 framework as well as an increase of the active site density may contribute to an easily decomposition of O_3 to get active oxygen species and to enhance the catalyst surface oxygen mobility enabling to specifically oxidize the different plasma generated hazardous gaseous species such as phosgene, trichloroacetaldehyde and dichloroacetylchloride. These characteristics explain the better performances of the NTP coupled with Fe-K-OMS-2 towards TCE abatement in our experimental conditions.

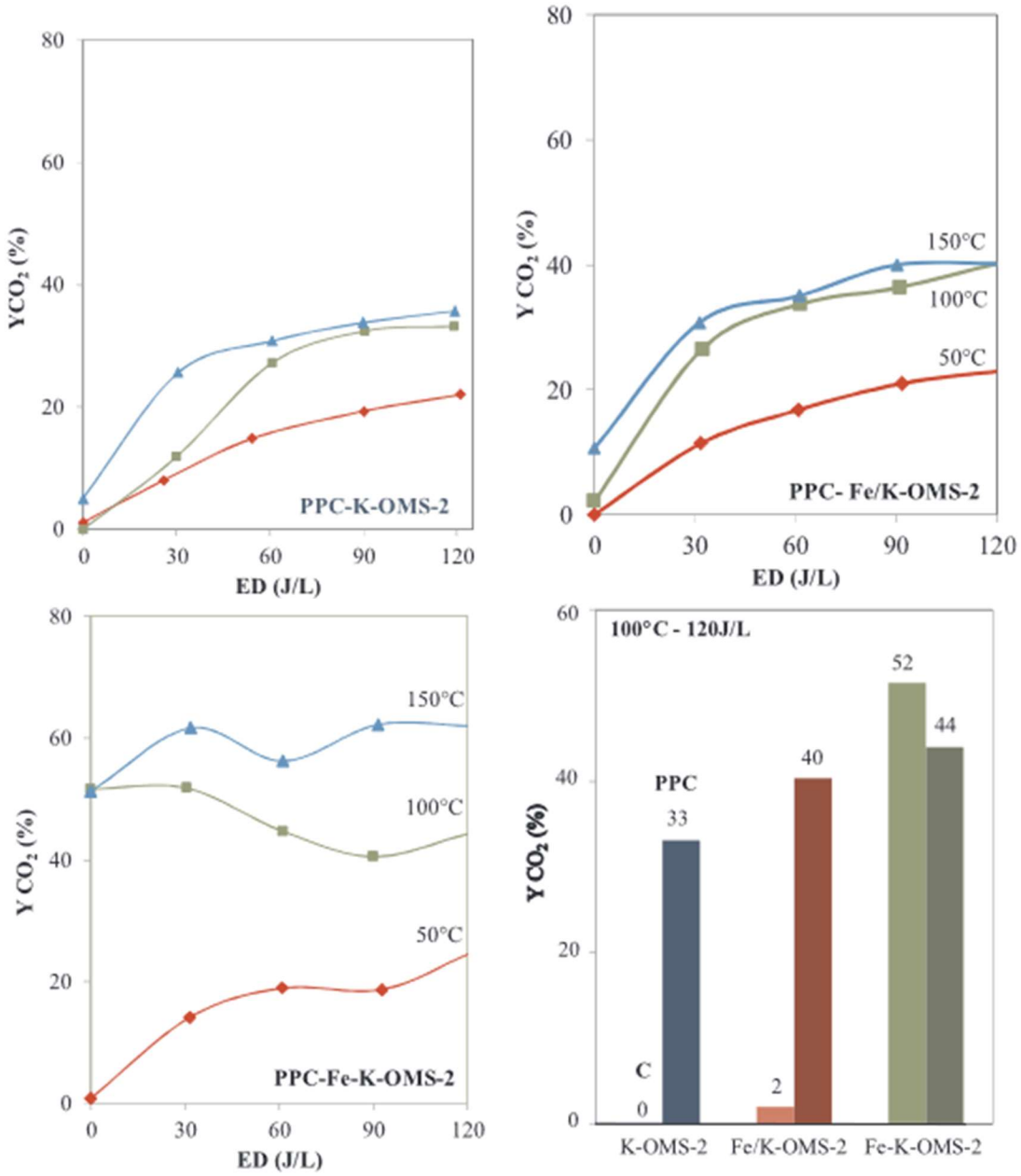

Fig. 9. CO_2 yields in PPC experiments as a function of ED and catalyst temperature.

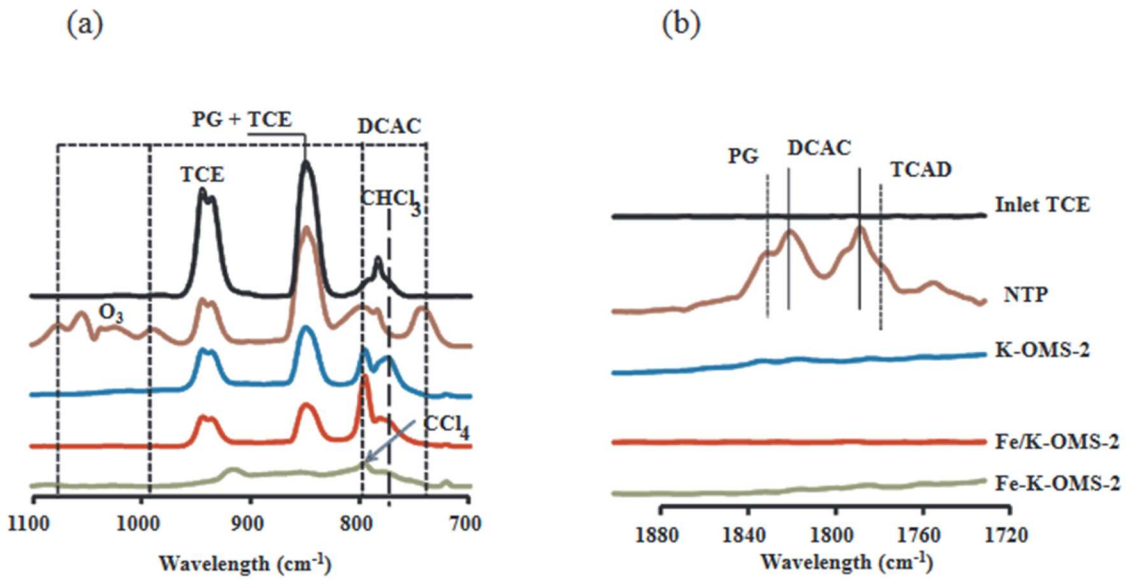

Fig. 10. FT-IR spectra between 1880 and 1700 cm−1 (a) and 1100 and 700 cm−1 (b) of inlet and outlet stream (Tc = 150 °C; ED = 90J/L; PG: Phosgene; DCAC: Dichloroacetylchloride; TCAD: Trichloroacetaldehyde).

5. Conclusion

Plasma assisted Fe-K-OMS-2 catalyst working in post-plasma configuration at a temperature of 150 °C presents high activity for TCE removal in moist air and relevant CO 2 yields. The improved performances of this material can be related to an increase of oxygen vacancies and oxygen mobility in comparison to those of the K-OMS-2 catalyst. These characteristics allow facilitating the production of active species from plasma generated ozone and the surface oxygen mobility to promote the degradation of VOC of intermediates of reaction into CO2.

Acknowledgments

The research has been partially supported by an Interreg V France-Wallonie-Vlaanderen project entitled “DepollutAir” and a PICS (Preparation of catalysts and catalytic depollution assisted by plasma) from CNRS is acknowledged for financial support. Chevreul Institute (FR 2638), Ministère de l’Enseignement Supérieur et de la Recherche, Région Nord − Pas de Calais and FEDER are acknowledged for supporting and funding this work. The authors are grateful in particular to Olivier Gardoll (Lille1 University, France) for the TPR analyses, Nora Djelal for SEM analysis, Laurence Burylo for XRD measurements, Dayan Chlala and Elise Bernier for Raman measurements.

References

[1] P. Vineis, F. Forastiere, G. Hoek, M. Lipsett, Inter. J. Cancer 111 (2004) 647–652.
[2] J. Van Durme, J. Dewulf, C. Leys, H. Van Langenhove, Appl. Catal. B Environ. 78 (2008) 324–336.
[3] H.L. Chen, H.M. Lee, S.W.H. Chen, M.B. Chang, S.J. Yu, S.N. Li, Environ. Sci. Technol. 43 (2009) 2216–2227.
[4] A.M. Vandenbroucke, R. Morent, N. De Geyter, C. Leys, J. Hazard. Mater. 195 (2011) 30–54.
[5] A.M. Vandenbroucke, R. Morent, N. De Geyter, C. Leys, J. Adv. Oxid. Technol. 14

(2011) 165–173.
[6] S.B. Han, T. Oda, R. Ono, IEEE Trans. Ind. Appl. 4 (2005) 1343–1349.
[7] S.B. Han, T. Oda, Plasma Sources Sci. Technol. 16 (2007) 413–421.
[8] B. Dhandapani, S.T. Oyama, Chem. Lett. 6 (1995) 413–414.
[9] J. Cai, J. Liu, W.S. Willis, S.L. Suib, Chem. Mater. 13 (2001) 2413–2422.
[10] J. Luo, Q. Zhang, J. Garcia-Martinez, S.L. Suib, J. Am. Chem. Soc. 130 (2008) 3198–3207.
[11] V.P. Santos, M.F.R. Pereira, J.J.M. Órfão, J.L. Figueiredo, Top. Catal. 52 (2009) 470–478.
[12] V.P. Santos, M.F.R. Pereira, J.J.M. Órfão, J.L. Figueiredo, Appl. Catal. B Environ. 88 (2009) 550–556.
[13] V.P. Santos, M.F.R. Pereira, J.J.M. Órfão, J.L. Figueiredo, Appl. Catal. B Environ. 99 (2010) 353–363.
[14] L. Lamaita, M.A. Peluso, J.E. Sambeth, H. Thomas, G. Mineli, P. Porta, Catal. Today 107-08 (2005) 133–138.
[15] L. Lamaita, M.A. Peluso, J.E. Sambeth, H.J. Thomas, Appl. Catal. B-Environ.61 (2005) 114-119.
[16] M.A. Peluso, L.A. Gambaro, E. Pronsato, D. Gazzoli, H.J. Thomas, J.E. Sambeth, Catal. Today 133–135 (2008) 487–492.
[17] S.L. Suib, J. Mater. Chem. 18 (2008) 1623–1631.
[18] M.A. Peluso, E. Pronsato, J.E. Sambeth, H.J. Thomas, G. Busca, Appl. Catal. B Environ. 78 (2008) 73–79.
[19] A.M. Vandenbroucke, M. Mora, C. Jiménez-Sanchidrián, F.J. Romero-Salguero, N. De Geyter, C. Leys, R. Morent, Appl. Catal. B Environ. 156 (2014) 94–100.
[20] M.T. Nguyen Dinh, J.-M. Giraudon, A.M. Vandenbroucke, R. Morent, N. De Geyter, J.-F. Lamonier, J. Hazard. Mater. 314 (2016) 88–94.
[21] W.-N. Li, J. Yuan, X.-F. Shen, S.G. Mower, L.-P. Xu, S. Sithambaram, M. Aindow, S.L. Suib, Adv. Funct. Mater. 16 (2006) 1247–1253.
[22] T. Sriskandakumar, N. Opembe, C.-H. Chen, A. Morey, C. King'ondu, S.L. Suib, J. Phys. Chem. A 113 (2009) 1523–1530.
[23] X. Chen, Y.-F. Shen, S.L. Suib, C.L. O'Young, Chem. Mater. 14 (2002) 940–948.
[24] C.K. King'ondu, N. Opembe, C.-H. Chen, K. Ngala, H. Huang, A. IyerH, H.F. Garcés, S.L. Suib, Adv. Funct. Mater. 21 (2011) 312–323.
[25] M. Polverejan, J.C. Villegas, S.L. Suib, J. Am. Chem. Soc. 126 (2004) 7774–7775.
[26] X. Shen, A.M. Morey, J. Liu, Y. Ding, J. Cai, J. Durand, Q. Wang, W. Wen, W.A. Hines, J.C. Hanson, J. Bai, A.I. Frenkel, W. Reiff, M. Aindow, S.L. Suib, J. Phys. Chem. C 115 (2011) 21610–21619.
[27] C. Calvert, R. Joesten, K. Ngala, J. Villegas, A. Morey, X. Shen, S.L. Suib, Chem. Mater. 20 (2008) 6382–6388.
[28] J. Chen, X. Tang, J. Liu, E. Zhan, J. Li, X. Huang, W. Shen, Chem. Mater. 19 (2007) 4292–4299.
[29] X. Tang, J. Li, J. Hao, Catal. Commun. 11 (2010) 871–875.
[30] L. Sun, Q.Q. Cao, B.Q. Hu, J.H. Li, J.M. Hao, G.H. Jing, X.F. Tang, Appl. Catal. A: Gen. 393 (2011) 323–330.
[31] Z. Lian, J. Ma, H. He, Catal. Comm. 59 (2015) 156–160.
[32] Q. H.Trinh, Y.S. Mok, Catalysts 5 (2015) 800–814.
[33] M. Sun, L. Yu, F. Ye, G. Diao, Q. Yu, Z. Hao, Y. Zheng, L. Yuan, Chem. Eng. J. 220 (2013) 320–327.
[34] H. Yin, X. Dai, M. Zhu, F. Li, X. Feng, F. Liu, H. Yin, J. Hazard. Mater. 296 (2015) 221–229.
[35] T. Zhang, X. Zhang, J. Ng, H. Yang, J. Liu, D. Delai Sun, Chem. Commun. 47 (2011) 1890–1892.
[36] M.T. Nguyen Dinh, J.-M. Giraudon, J.-F. Lamonier, A. Vandenbroucke, N. De

Geyter, C. Leys, R. Morent, Appl. Catal. B Environ. 147 (2014) 904–911.
[37] A.M. Vandenbroucke, D. Minh Tuan Nguyen, J.-M. Giraudon, R. Morent, N. De Geyter, J.-F. Lamonier, C. Leys, Plasma Chem. Plasma Process. 31 (2011) 707–718.
[38] J. Luo, Q. Zhang, A. Huang, S.L. Suib, Microporous Mesoporous Mater. 35–36 (2000) 209–217.
[39] V.P. Santos, M.F.R. Pereira, J.J.M. Órfão, J.L. Figueiredo, J. Hazard. Mater. 185 (2011) 1236–1240.
[40] I. Attibak, A. Bueno-Lopez, A. Garcia-Garcia, P. Navaro, D. Frias, M. Montes, Appl. Catal. B 93 (2010) 267.
[41] Y.G. Yin, W.Q. Xu, S.L. Suib, Inorg. Chem. 34 (1995) 4187.
[42] T. Gao, M. Glerup, F. Krumeich, R. Nesper, H. Fjellvåg, P. Norby, J. Phys. Chem. C 112 (2008) 13134.
[43] T. Chen, H. Dou, X. Li, X. Tang, J. Li, J. Hao, Microporous Mesoporous Mater. 122 (2009) 270–274.
[44] W.Y. Hernándeza, M.A. Centenoa, S. Ivanovaa, P. Eloyb, E.M. Gaigneaux, J.A. Odriozolaa, Appl. Catal. B 123 (2012) 27.
[45] F. Kapteijn, L. Singoredjo, A. Andreini, Appl. Catal. B 3 (1994) 173.
[46] S. Said, M. Riad, M. Helmy, S. Mikhai, L. Khalil, J. Nanostruct. Chem. 6 (2016) 171–182.
[47] Y.F. Shen, S.L. SuibC, L. O'Young, J. Am.Chem.Soc 116 (1994) 11020.
[48] R. Morent, C. Leys, Ozone Sci. Eng. 27 (2005) 239.
[49] B. Eliasson, M. Hirth, U. Kogelschatz, J. Phys. D Appl. Phys. 20 (1987) 1421.